symmetry

IMPACT FACTOR 2.2

CITESCORE 5.4

Article

Charging and Discharging Modeling of Inertial Sensors Based on Ultraviolet Charge Management

Zihan Zhao, Tao Yu, Shang Wang, Huadong Li and Zhi Wang

MDPI

https://doi.org/10.3390/sym16091209

symmetry

MDPI

Article

Charging and Discharging Modeling of Inertial Sensors Based on Ultraviolet Charge Management

Zihan Zhao [1,2], Tao Yu [1,*], Shang Wang [1], Huadong Li [1] and Zhi Wang [1,3,*]

[1] Changchun Institute of Optics, Fine Mechanics and Physics, Chinese Academy of Sciences, Changchun 130033, China; zhaozihan22@mails.ucas.ac.cn (Z.Z.); ws790402497@163.com (S.W.); lihuadong@ciomp.ac.cn (H.L.)
[2] University of Chinese Academy of Sciences, Beijing 100049, China
[3] School of Fundamental Physics and Mathematical Sciences, Hangzhou Institute for Advanced Study, University of Chinese Academy of Sciences, Hangzhou 310024, China
* Correspondence: yut@ciomp.ac.cn (T.Y.); wz070611@126.com (Z.W.)

Abstract: Inertial sensors act as inertial references in space gravitational wave detection missions, necessitating that their internal test mass (TM) maintains minimal residual acceleration noise. High-energy particles and cosmic rays in space, along with ion pumps in ground-based torsion pendulum experiments, can cause charge accumulation on the TM surface, leading to increased residual acceleration noise. Consequently, a charge management system was introduced to control the TM's charge. The complex light path propagation within the electrode housing (EH) makes the TM's charging and discharging process difficult to theoretically calculate and fully simulate. To address this issue, we propose a simulation method for charging and discharging inertial sensors within ultraviolet (UV) charge management systems. This method innovatively considers the impact of photoelectron emission angle and the TM's position offset from symmetry on performance. The method also simulates charging and discharging rates over time under conditions of symmetry and preliminarily examines factors affecting the TM's equilibrium potential. Simulation results indicate that this method effectively models the charge management system's operation, providing a valuable reference for system design.

Keywords: inertial sensors; charge management system; UV discharge

Citation: Zhao, Z.; Yu, T.; Wang, S.; Li, H.; Wang, Z. Charging and Discharging Modeling of Inertial Sensors Based on Ultraviolet Charge Management. *Symmetry* **2024**, *16*, 1209. https://doi.org/10.3390/sym16091209

Academic Editors: Christophe Humbert and Raffaele Barretta

Received: 5 August 2024
Revised: 3 September 2024
Accepted: 12 September 2024
Published: 14 September 2024

1. Introduction

The fundamental principle underlying space-based gravitational wave detection is the use of inertial sensors as end mirrors within a high-precision inter-satellite interferometer. This interferometer measures variations in the relative positions of TM within two spatially separated satellites to detect gravitational wave signals [1–3]. The inertial sensor, comprising a TM, an EH, and associated peripherals, is critical for space-based gravitational wave detection [4–6]. Therefore, the residual acceleration of the inertial sensor must be confined to 10^{-15} m/s^2/Hz$^{1/2}$, necessitating rigorous control of non-conservative force interference on the TM.

However, high-energy particles and cosmic rays in space continuously bombard the spacecraft, leading to charge accumulation on the TM surface via both direct and indirect mechanisms [7–9]. This charge buildup can induce additional coupling forces between the TM and its surrounding structure, thereby compromising the precision of gravitational wave detection [10]. During solar minimum periods, the TM charging rate due to galactic cosmic rays can reach 39.5 e/s [11], while the charging rate induced by solar energetic particles can exceed 1.6×10^4 e/s [12,13]. Moreover, ion pumps employed to maintain high-vacuum conditions in the torsion pendulum system can cause rapid charge accumulation on the TM surface [14–16]. Once the TM accumulates 10^7 e, the resultant acceleration noise will surpass the specified limits of the inertial sensor.

Thus, a charge management system is essential to stabilize residual charge on the TM surface, mitigate Coulomb forces arising from charge accumulation, and minimize Lorentz forces resulting from magnetic coupling, thereby ensuring that residual acceleration noise adheres to mission requirements.

Currently, the majority of research teams employ UV light to charge and discharge the TM [17,18]. This approach, when compared to alternative methods, does not introduce additional acceleration noise, is straightforward to implement, and offers high controllability, positioning it as the most promising technology for charge management [19].

In recent years, various simulation studies have explored charge accumulation and management challenges in space-based inertial sensors. In 2011, Daniel Hollington of Imperial College London utilized Geant4 software Geant4-11.2.2 to simulate charge accumulation and charge management within the inertial sensors of the LISA Pathfinder (LPF) spacecraft. His study identified substantial discrepancies between simulation results in the space environment and experimental data [20]. In 2020, Fangchao Yang from Huazhong University of Science and Technology similarly employed Geant4 software to simulate the charge accumulation rate and assess the performance of the charge management system in the TianQin project spacecraft. He also conducted an analysis of the discharge rates of inertial sensors under alternating current discharge conditions [21]. In 2014, Tobias Ziegler and his team developed ray tracing and electron tracking software to simulate the quality of UV Light-Emitting Diode (LED) exposure and the motion of photoelectrons in the LPF mission [22]. They further analyzed the discharge curves of the charge management system and proposed optimizations.

To evaluate the charge management system prior to the development of a torsion pendulum prototype, it is imperative to construct a simulation model of the torsion pendulum configuration. This model will serve as the theoretical foundation for the subsequent construction of a ground-based torsion pendulum UV charge management system prototype. Current research presents limitations in precisely predicting charge and discharge behaviors. Consequently, it is crucial to develop a simulation model that accurately represents UV light propagation and photoelectron transport, thereby optimizing the design and performance of the charge management system.

In summary, this study will employ ray tracing software to determine the parameters influencing UV light propagation within the inertial sensor, drawing on experimental data and the literature. It will simulate UV light reflection and absorption within the sensor to quantify UV light absorption by different surfaces. Subsequently, it will model photoelectron transmission inside the sensor, utilizing equations for kinetic energy, azimuth angle, and polar angle distribution, to determine the TM charging and discharging rates. Finally, the established simulation model will be used to simulate the direct current (DC) charging and discharging dynamics of the inertial sensor and analyze these rates during charge management, including symmetry-based tests to evaluate both charging and discharging performance.

Additionally, in the ground-based torsion pendulum charge management system, the TM may drift over time due to the unwinding of tungsten fibers, thereby altering UV light propagation within the inertial sensor. Notably, previous simulation models have not accounted for the impact of TM positional offset on charging and discharging performance. To assess the impact of this phenomenon on the TM's charging and discharging rates, this study will utilize the charge management simulation model to simulate rate variations at various offset positions of symmetry on the TM surface, providing a quantitative analysis.

A key contribution of this research is the pioneering simulation of the TM's offset position within the charge management system, which considers the influence of photoelectron emission angles on the TM's charging and discharging rates. This approach provides precise insights into how positional deviations impact these rates. This innovation offers a robust theoretical foundation and technical support for future research on charge management systems while ensuring the model's high adaptability. The model is equally applicable to ground-based torsion pendulum experiments and future space-based

gravitational wave detection missions, providing essential theoretical support for practical applications in these fields.

2. Establishment of the TM Charging and Discharging Model

To accurately simulate the charge management system employed in ground-based torsion pendulum experiments, this chapter first establishes the configuration of the inertial sensor and performs detailed 3D modeling. The optical parameters of the EH and TM are then meticulously determined to ensure precise light path propagation within the inertial sensor. These parameters are subsequently utilized as inputs for ray tracing simulations. Following ray tracing analysis, the photon flux on the surfaces of the TM and EH, as well as their corresponding discrete distribution functions, is quantified.

Finally, the trajectories and dynamics of photoelectrons within the EH are rigorously analyzed and simulated. A comprehensive photoelectron flow model is developed to simulate the movement of photoelectrons within the EH, allowing for precise determination of the photoelectron count involved in the charging and discharging processes of the TM.

2.1. Three-Dimensional Modeling of the TM and EH

The inertial sensor configuration described in this paper is derived from the LPF mission [23]. The key distinction is that the ground-based TM lacks the corner holes required for the locking release pin structure and instead features a central fixing mechanism for the suspension wire.

The TM is a 46 mm × 46 mm Au-plated conductor, and has symmetry. When centrally positioned, the gap between its edges and the EH is either 2.9 mm or 4 mm [24], as illustrated in Figure 1a. In accordance with project specifications, four through-holes are fabricated at the edge of the EH to accommodate UV fibers. Two of these holes are oriented towards the TM surface, while the other two are directed at the EH surface, with the illumination points arranged in a configuration of central symmetry. The modeled representations of the TM and EH are depicted in Figure 1b (with the central connecting rod hidden).

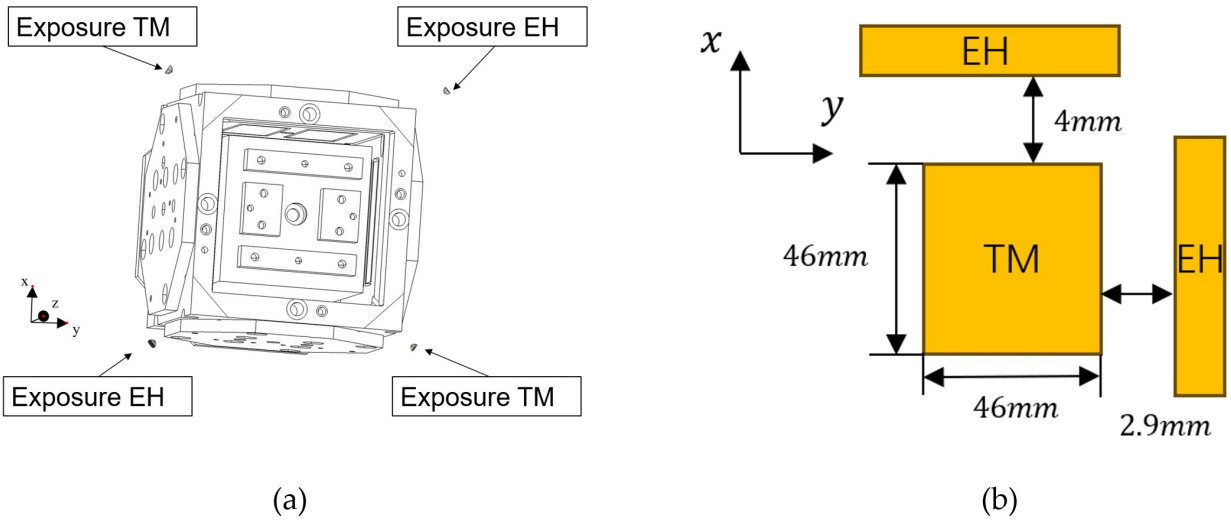

Figure 1. (**a**) The spacing between the TM and the EH in the x and y directions. (**b**) The illumination method of the inertial sensor.

2.2. UV Light Path Tracing

In the charge management system, UV light from the UV LED is focused by a lens into a UV optical fiber, which then directs the light onto the TM or EH surface [25], as shown in Figure 2.

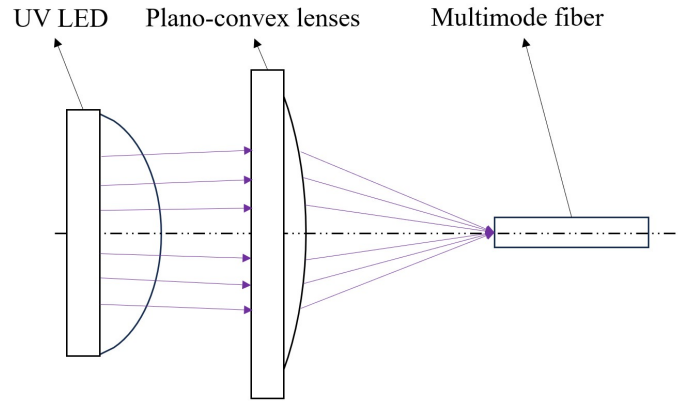

Figure 2. The convergence process of UV light.

To reduce performance differences due to inaccurate UV lens and fiber modeling, this paper uses a surface light source to simulate the UV light emitted from the fiber output during ray tracing.

When UV light passes through the optical fiber, factors like mode field distribution cause a non-uniform light distribution at the fiber output, describable by a Gaussian or quasi-Gaussian distribution. In a Gaussian distribution [26], optical power is concentrated at the center of the light cone, and its power distribution $P(r)$ is described as follows:

$$P(r) = P_0 e^{-\left(\frac{2r}{\gamma}\right)^2}, \quad (1)$$

where P_0 is the maximum optical power, r is the radial distance from the center, and γ is the Gaussian radius. The Gaussian radius contains 86.5% of the UV optical power. Thus, measuring the divergence angle at the UV fiber output can simulate the light distribution at the fiber output. All the symbols and their meanings used in the formulas in this paper are listed in Table A1.

During the experiment, the fiber output was securely mounted on a bracket, while the optical power meter was positioned on a micro-positioning stage. A light-blocking plate with a precision aperture was placed directly in front of the fiber output, as illustrated in Figure 3. The UV LED was operated at an elevated power level, and the micro-positioning stage was adjusted to laterally translate the optical power meter, thereby determining the radial distance at which the optical power reaches $\frac{P_0}{2}$.

When using ray tracing software to simulate light path propagation inside the EH, it is necessary to determine the optical parameters of the TM and EH based on experiments, ensuring the light propagates as it would in a real environment.

This paper defines the optical parameters inside the EH based on experimental data from LPF.

The optical parameters affecting the transmission of UV light inside the EH are shown in Table 1.

Table 1. Optical parameters for ray tracing [20,21].

Parameter	Value
Au Conductor Refractive Index	$N = 1.296, k = 1.696$
Au-Pt Alloy Refractive Index	$N = 1.32, k = 1.74$
Reflection Type	Specular, Diffuse
Reflection Distribution	20% Specular, 80% Diffuse
UV Fiber Output Angle	12°

The complex refractive indices of Au conductors and Au-Pt alloy conductors dictate their UV light absorption properties, thereby influencing the reflection dynamics as UV light traverses different media. The specific type of reflection governs the manner in which UV light is reflected within the EH, subsequently affecting the precise locations of UV irradiation post-reflection. The distribution of reflections dictates the proportionate occurrence of each reflection type.

After ray tracing, the photon flux size on the surfaces of the TM and EH, along with the discrete distribution function of the photon flux, can be obtained.

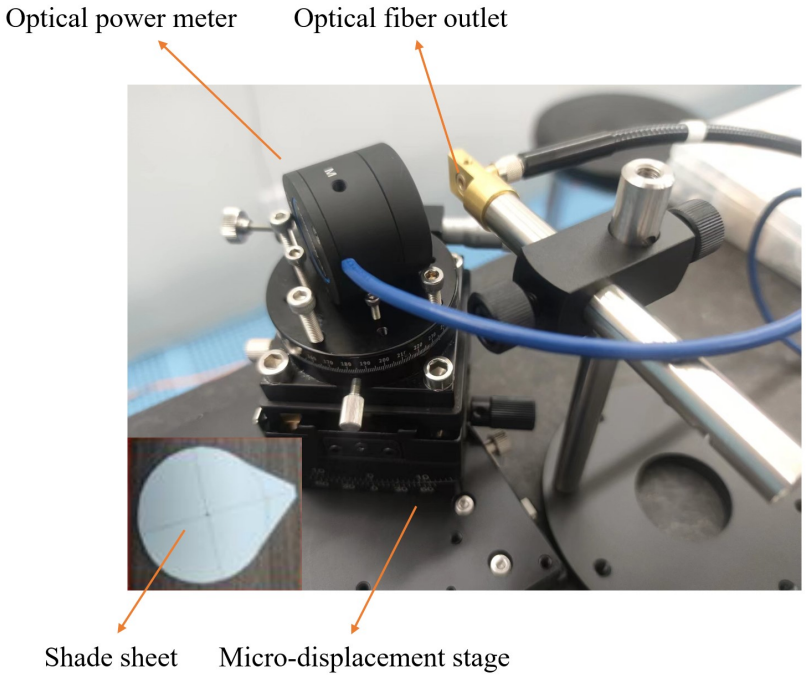

Figure 3. Divergence angle calibration experiment of the optical fiber output port.

2.3. Physical Characteristics Analysis of the TM and EH

After UV light irradiates the inside of the EH, the Au-plated conductor surface will emit photoelectrons due to the photoelectric effect. The emission location of the photoelectrons varies depending on the UV irradiation position. As shown in Figure 4, some photoelectrons emitted from the EH can transfer to the TM surface (blue photoelectrons); however, others cannot charge the TM due to insufficient initial kinetic energy or emission angle (green photoelectrons).

Therefore, this paper considers the effects of the initial kinetic energy and emission angle of photoelectrons on the charge and discharge rate of the charge management system during simulation. The initial state of photoelectron emission is described using the parameters in Table 2, with reference to Figure 5.

Table 2. Initial properties of photoelectrons.

Name	Symbol	Unit
Initial Kinetic Energy	E	Electron Volt (eV)
Polar Angle	θ	Degree (°)
Azimuth Angle	φ	Degree (°)

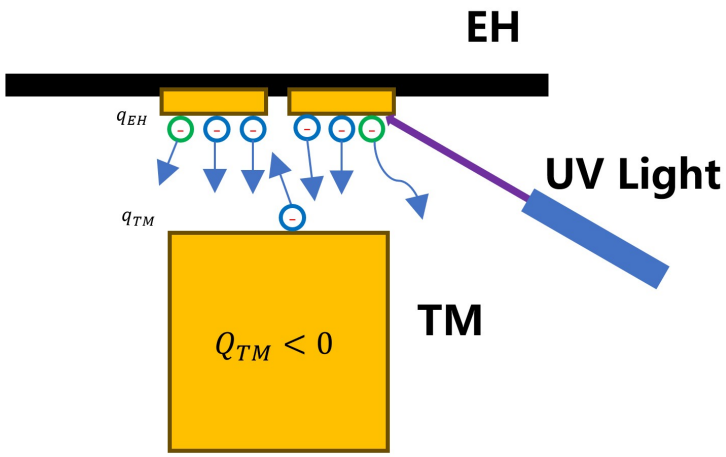

Figure 4. The state of photoelectron escape.

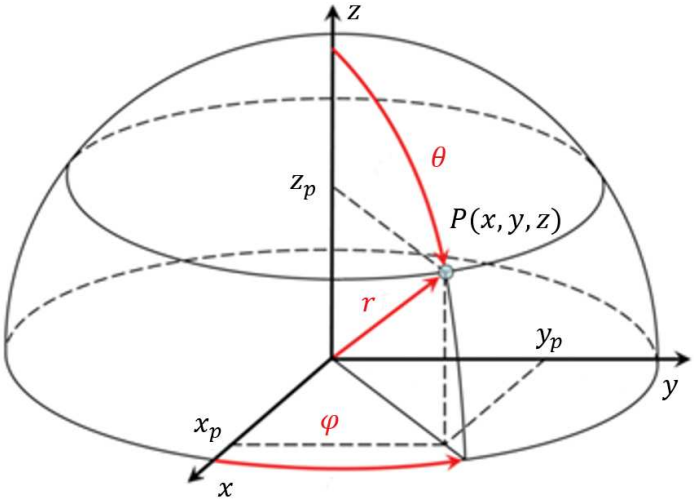

Figure 5. The angular distribution state of photoelectron emission.

The polar angle θ is the angle between the emission position and the Z axis, and the azimuth angle is the angle between the photoelectron's projection on the X-Y plane and the X axis.

The LPF team has described the normal initial kinetic energy of photoelectrons during emission [27], but has not provided an expression for the angular distribution of photoelectrons during emission. This paper adopts Wu Chuan-Teh's theory on the initial kinetic energy and polar angle distribution of photoelectrons to describe their state during emission [28].

The initial kinetic energy distribution function of the photoelectrons is

$$p(E)dE = c_1 \frac{E - \omega\left(1 - e^{-\frac{E}{\omega}}\right)}{1 + e^{\frac{E - E_m}{kT}}} dE, \tag{2}$$

where E represents the initial kinetic energy of the photoelectron upon escape; E_m is the maximum initial kinetic energy the photoelectron can have; $c_1 = c\frac{4\pi m}{h^3}$; c is a parameter related to factors such as incident light frequency and intensity, with a value of $0 < c < 1$; h is Planck's constant; m is the electron mass; ω is a parameter related to the metal reflection effect; T is the absolute temperature; and k is the Boltzmann constant.

The polar angle distribution function of the photoelectrons is

$$p(\theta)d\theta = \left(c_1 k^2 T^2 \frac{\mu^2}{2} + \frac{\pi^2}{6} + \frac{\mu e^{-\mu \frac{kT}{\omega} \cos^2\theta}}{\frac{kT}{\omega} \cos^2\theta} - \frac{1 - e^{-\mu \frac{kT}{\omega} \cos^2\theta}}{\left(\frac{kT}{\omega}\right)^2 \cos^4\theta} \right) 2 \sin\theta \cos\theta d\theta, \quad (3)$$

where θ represents the polar angle of the photoelectron at the time of emission, $\mu = \frac{E_m}{kT}$, e is the natural constant, and the remaining symbols have the same meanings as in Equation (2).

The azimuth angle distribution of the photoelectrons is assumed to be uniformly distributed.

After the ray tracing in Section 2.2, the discrete distribution function of the photon flux on the conductor surface, $f(dx, dy)$, can be obtained, with the total photon flux on the conductor surface being PF_{total} (in units of μmol/s). Assuming the probability density function (PDF) of the photon flux distribution on the conductor surface is $PDF_{dx,dy}$, then

$$\mathrm{PDF}_{dx,dy} = \frac{f(dx, dy)}{\mathrm{PF}_{\mathrm{total}}}. \quad (4)$$

Therefore, the initial position of each photoelectron based on the $PDF_{dx,dy}$ of the photon flux distribution on the conductor surface can be selected. Additionally, this study uses the UV lamp photon energy and the conductor surface work function reported by David DAL Bosco from the University of Trento, setting them to 4.88 eV and 3.9 eV, respectively [20]. Thus, the maximum initial kinetic energy of the photoelectrons is 0.98 eV. At this point, all conditions necessary for simulating the trajectories of photoelectrons are met, as shown in Table 3.

Table 3. All initial parameters required to simulate the motion of photoelectrons.

Variable Name	Variable Source
Kinetic Energy E	Equation (2)
Maximum Initial Kinetic Energy E_{max}	Reference [24]
Polar Angle θ	Equation (3)
Azimuth Angle φ	Uniformly Distributed
Initial Position	Equation (4)

The velocity of the photoelectron upon emission, V_0, is

$$V_0 = \sqrt{\frac{2E}{m}}, \quad (5)$$

where m represents the mass of the photoelectron.

The velocities of the photoelectron in the x, y, and z directions are defined as V_{0x},V_{0y}, and V_{0z}, respectively, and can be calculated as follows:

$$\begin{cases} V_{0x} = V_0 \sin\theta \cos\varphi \\ V_{0y} = V_0 \sin\theta \sin\varphi \\ V_{0z} = V_0 \cos\theta \end{cases}. \quad (6)$$

2.4. Photoelectron Flow Model

When UV light irradiates the interior of the EH, a simple mathematical model can represent the number of photoelectrons emitted from the surface:

$$N_e = N_p \times QY_{\mathrm{ext}}, \quad (7)$$

where N_e represents the number of photoelectrons, N_p represents the number of photons incident on the conductor surface, and QY_{ext} represents the quantum yield. In this simula-

tion, the quantum yield for the TM is set to 2.0×10^{-5} e/photon, and the quantum yield for the EH is set to 1.9×10^{-5} e/photon [21]. The value of N_p can be obtained through ray tracing.

After photoelectrons are emitted from the surface of the TM or the EH, they must overcome the electric field in the normal direction to transfer to the other surface.

The kinetic energy of the photoelectrons in the z direction, based on the velocity component V_{0z}, is calculated as follows:

$$E_z = \frac{mV_{0z}^2}{2}. \tag{8}$$

The work performed by the photoelectrons to overcome the electric field in the z direction is

$$E_{z'} = e \times U_D, \tag{9}$$

where e represents the charge, and U_D represents the potential difference between the TM and the EH.

If $E_z + Ez' > 0$, then the photoelectron satisfies the condition for transfer from the TM to the EH or from the EH to the TM in the z direction.

When a photoelectron is emitted from the EH, we must consider whether it can overcome the electric field and its direction of motion to determine if it can contribute to the charging of the TM, as shown in Figure 6.

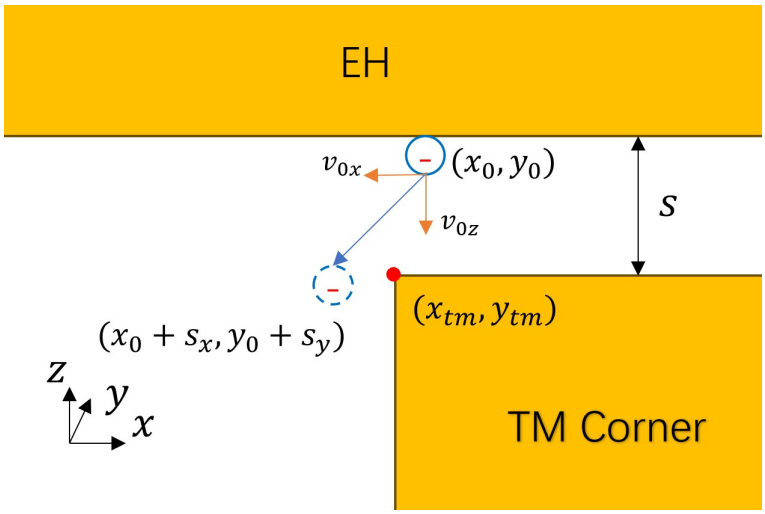

Figure 6. The initial and final positions of photoelectrons.

Assuming the position of the photoelectron upon emission is (x_0, y_0), the time t for the photoelectron to travel between the TM and the EH is calculated as

$$t = \frac{s}{V_{0z}}, \tag{10}$$

where s represents the distance between the TM and the EH.

The displacement of the photoelectron in the x and y directions, s_x and s_y, is calculated as

$$\begin{cases} s_x = V_{0x}t \\ s_y = V_{0y}t \end{cases}. \tag{11}$$

Let (x_{tm}, y_{tm}) be the coordinates of the corner position of the TM. If the position of the photoelectron emission on the EH satisfies the conditions in Equation (12), the photoelectron meets the transfer conditions from the EH to the TM in the x and y directions.

$$\begin{cases} x_0 + s_x < x_{tm} \\ y_0 + s_y < y_{tm} \end{cases} . \quad (12)$$

3. Verification of TM Charging and Discharging Performance

In Section 2, a three-dimensional model of the inertial sensor was constructed. The photon flux on the surfaces of the TM and the EH was obtained, and the initial positions of the photoelectrons were tracked. Based on the above simulations, this chapter will simulate the performance differences in the charge management system caused by the movement of the TM and the charge–discharge characteristics of the system.

3.1. Simulation of the Impact of TM Position Deviation on the Charge Management System

When the TM is displaced along the X axis or Y axis, the absorption and propagation of photons inside the EH change, altering the charge–discharge conditions and equilibrium potential of both the EH and the TM. When the TM is irradiated with UV LED, changes in the charge–discharge rate due to this phenomenon become more pronounced. However, when the EH is irradiated, since the position of the EH and its frame does not change, the displacement of the TM only affects photon absorption and photoelectron release by the TM.

To address these phenomena, this study uses the established charge management simulation model. The simulation conditions are shown in Table 4, and the offset positions of the TM have symmetry along the X axis and Y axis.

Table 4. Simulation parameters for the impact of TM position deviation on the performance of the charge management system.

Parameter	Value
TM X Position Deviation from Center	−4 mm +4 mm
TM Y Position Deviation from Center	−2.9 mm +2.9 mm
UV Light Power	60 nW

During the simulation, the TM is shifted by 0.1 mm in either the x or y direction each time, and the discharge data at each position are recorded, as shown in Figure 7.

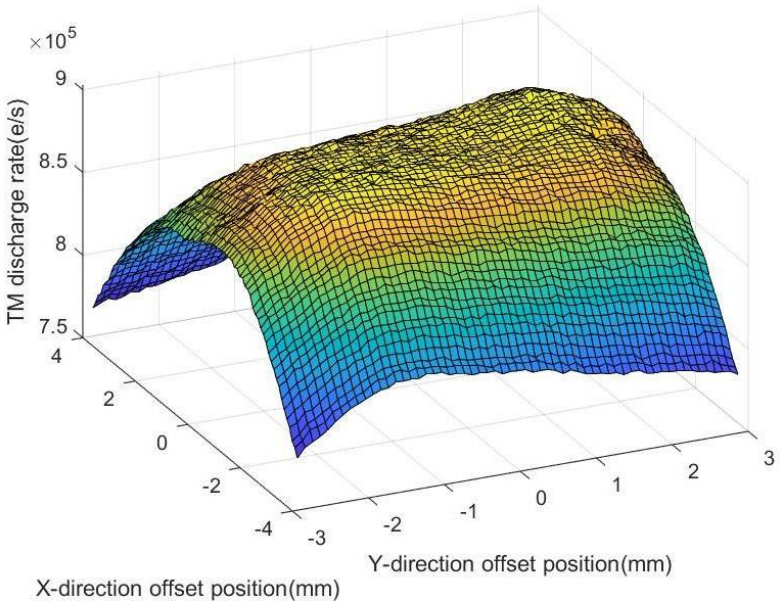

Figure 7. The impact of position offset on the performance of the charge management system. The colors in the figure, ranging from yellow to blue, represent a decreasing TM discharge rate.

When the TM position is shifted to (X = +0.8 mm, Y = +1.8 mm), the discharge rate of the TM reaches a maximum of approximately 9×10^5 e/s; when the TM position is shifted to (X = +4 mm, Y = −2.9 mm), the discharge rate of the TM reaches a minimum of only 7.6×10^5 e/s. The difference between the maximum and minimum discharge rates can reach 15%. However, during normal operation of the inertial sensor, the TM's deviation from the center position usually does not reach such a large extent. Within an interval of 0.1 mm, displacement of the TM position does not significantly affect the performance of the charge management system.

3.2. Simulation of TM Charging and Discharging Performance

When simulating the charge–discharge performance of the TM, this study treats the conductors as parallel-plate capacitors and neglects edge effects on charge movement. Using the simulation test parameters for the charge management system from reference [21], this study performs simulation analysis for both negatively and positively charged TM.

To discuss the charge–discharge simulation results, this study first analyzes the effect of the relative potential between the TM and the EH on the charge–discharge rate of the TM.

Based on the UV light energy settings and the conductor surface work function in Section 2, the maximum initial kinetic energy of photoelectrons is 0.98 eV. Define the surface potential of the TM as U_{TM}, the surface potential of the EH as U_{EH}, and the potential difference as follows:

$$U_D = U_{TM} - U_{EH}. \tag{13}$$

Since the electric field between the TM and the EH is considered uniformly distributed in this simulation, when U_D is greater than 0.98 V or less than −0.98 V, all electrons flowing between the TM and the EH cannot overcome the work performed by the electric field.

Suppose the charging rate from the EH to the TM is $\lambda(Q_{Charge})$ and the discharging rate from the TM to the EH is $\lambda(Q_{Discharge})$ when $U_D = 0\,V$; and suppose the charging rate from the EH to the TM is $V(Q_{Charge})$. The discharging rate from the TM to the EH is $V(Q_{Discharge})$ at a certain potential difference. Then, we have the following:

$$\begin{cases} \mathcal{A} \\ \mathcal{B} \\ \mathcal{C} \\ \mathcal{D} \end{cases} = \begin{cases} V(Q_{Discharge}) = \lambda(Q_{Discharge}), V(Q_{Charge}) = 0, U_D < -0.98\,V \\ V(Q_{Discharge}) = \lambda(Q_{Discharge}), 0 < V(Q_{Charge}) < \lambda(Q_{Charge}), -0.98\,V < U_D < 0\,V \\ 0 < V(Q_{Discharge}) < \lambda(Q_{Discharge}), V(Q_{Charge}) = \lambda(Q_{Charge}), 0\,V < U_D < 0.98\,V \\ V(Q_{Discharge}) = 0, V(Q_{Charge}) = \lambda(Q_{Charge}), 0.98\,V < U_D \end{cases}. \tag{14}$$

Four states are defined as $\mathcal{A}$, $\mathcal{B}$, $\mathcal{C}$, and $\mathcal{D}$.

When the TM is negatively charged, the simulation parameters are set as shown in Table 5.

Table 5. Initial simulation parameters for negatively charged TM.

Parameter	Value
EH Potential	0 V
TM Potential	−2.5 V
UV Light Power	30 nW
Residual Charge on TM	$5.34 \times 10^8\,e$

After the simulation, the potential variation on the TM surface and its discharging rate were obtained, as shown in Figure 8.

As shown in Figure 8a, when the TM carries a negative charge and is irradiated, its surface potential reaches an equilibrium state after 2500 s, with an equilibrium potential of approximately 0.85 V. In Figure 8b, before 680 s, the potential difference is less than −0.98 V, corresponding to state $\mathcal{A}$, with a discharge rate of 2.3 mV/s. At 680 s, the potential difference exceeds −0.98 V, corresponding to state $\mathcal{B}$, and the discharge rate of the TM begins to decline. At 1130 s, the potential difference reaches 0 V, and the charging and

discharging of the TM are not inhibited. At this time, the number of electrons flowing from the TM to the EH and from the EH to the TM per unit time both reach their maximum, with the TM discharging at a rate of 2.1 mV/s. After 1130 s, the potential difference becomes greater than 0 V, corresponding to state $\mathcal{C}$, causing the discharge rate to gradually decrease until around 2500 s, when the electron flow between the TM and the EH is balanced and the TM reaches equilibrium potential.

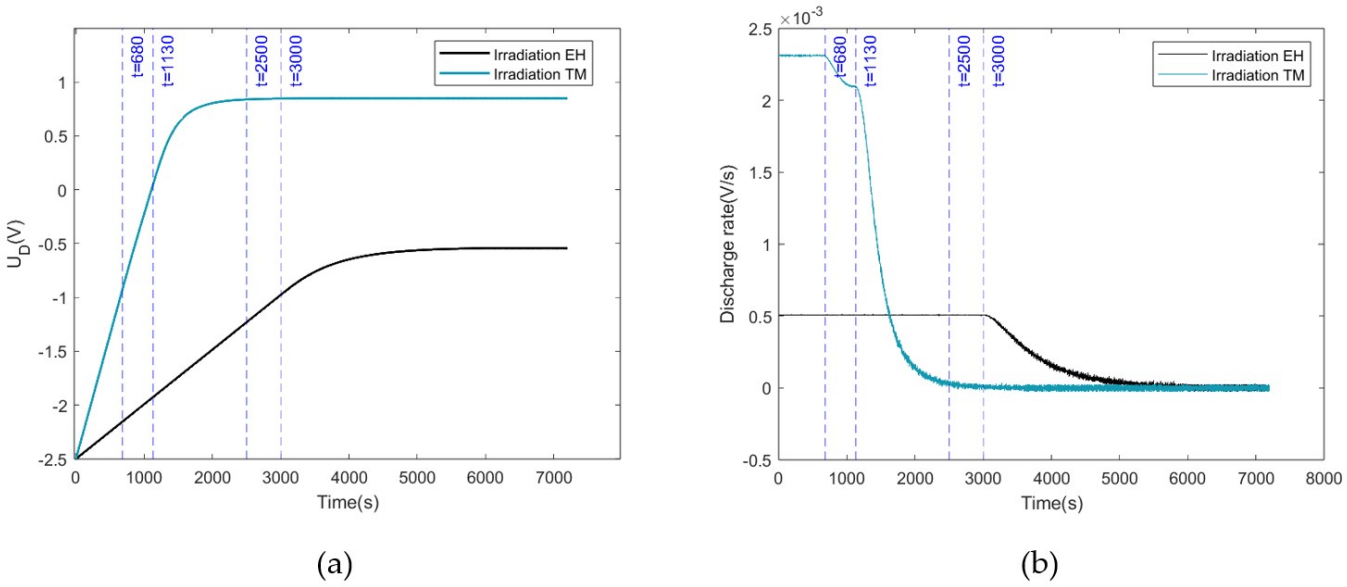

Figure 8. Simulation results of charge management performance when the TM is negatively charged. (**a**) Change in potential difference. (**b**) Change in discharge rate of TM.

When irradiating the EH, before 3000 s, the potential difference is less than −0.98 V, corresponding to state $\mathcal{A}$, with the TM discharging at a rate of 0.5 mV/s. At 3000 s, the potential difference reaches −0.98 V, corresponding to state $\mathcal{B}$, and the discharge rate begins to decrease until around 6000 s, when electron flow is balanced and the TM reaches an equilibrium potential of −0.53 V.

With symmetry, the state of the positively charged TM was simulated, with parameters set as shown in Table 6.

Table 6. Initial simulation parameters for positively charged TM.

Parameter	Value
EH Potential	0 V
TM Potential	+2.5 V
UV Light Power	30 nW
Residual Charge on TM	$-5.34 \times 10^8\, e$

The performance simulation results are shown in Figure 9.

As shown in Figure 9a, when the TM carries a positive charge and the EH is irradiated, its surface potential reaches an equilibrium state after 7500 s, with an equilibrium potential of approximately −0.53 V. In Figure 9b, before 1750 s, the potential difference is greater than 0.98 V, corresponding to state $\mathcal{D}$, with a charging rate of 0.88 mV/s. At 1750 s, the potential difference drops below 0.98 V, corresponding to state $\mathcal{C}$, and the charging rate of the TM begins to decrease. At 3800 s, the potential difference reaches 0 V, and the charging and discharging of the TM are not inhibited. At this time, the number of electrons flowing from the TM to the EH and from the EH to the TM per unit time both reach their maximum, with the TM charging at a rate of 0.37 mV/s. After 3800 s, the potential difference becomes greater than 0 V, corresponding to state $\mathcal{B}$, causing the charging rate to gradually decrease

until around 7500 s, when the electron flow between the TM and the EH is balanced and the TM reaches equilibrium potential.

When the TM is irradiated, before 7100 s, the potential difference is greater than 0.98 V, corresponding to state $\mathcal{D}$, with the TM charging at a rate of 0.21 mV/s. At 7100 s, the potential difference reaches 0.98 V, corresponding to state $\mathcal{C}$, and the charging rate begins to gradually decrease until around 8700 s, when electron flow is balanced and the TM reaches an equilibrium potential of 0.85 V.

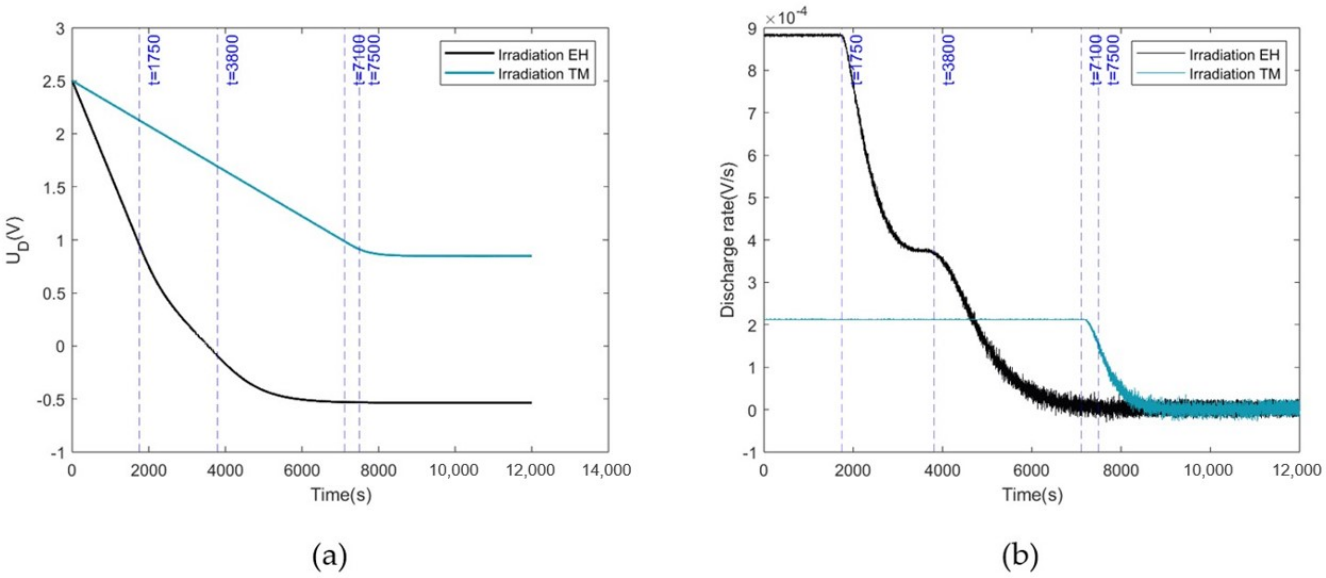

Figure 9. Simulation results of charge management performance when the TM is positively charged. (**a**) Change in potential difference. (**b**) Change in charge rate of TM.

Comparing the discharging results of the TM with initial positive and negative charges, the equilibrium potential eventually reaches 0.85 V when the TM is irradiated, while it reaches −0.53 V when the EH is irradiated. Without applying a bias voltage, regardless of the initial charge, simply using UV light to irradiate the TM or the EH will eventually bring the TM to the same equilibrium potential. The equilibrium potential of the TM is determined by the matching rates of charging from the EH to the TM and discharging from the TM to the EH. Therefore, any factor causing asymmetry changes in the charging and discharging rates of the TM will affect the equilibrium potential, such as the angle of UV irradiation and changes in the work function of the conductor surface due to air pollution.

The study in [21] provides the charge–discharge rate and the magnitudes of the positive and negative balance potentials. These are compared to the simulation results obtained in this paper, as shown in Table 7.

Table 7. TM charge and discharge simulation results, and experimental results.

Parameter	Simulation Value	Literature [21] Simulation Value	Experimentalt Value
Max Discharge Rate	2.3 mV/s	2.3 mV/s	2.61 ± 0.03 mV/s
Max Charge Rate	0.88 mV/s	2.5 mV/s	0.88 ± 0.02 mV/s
Positive Equilibrium Potential	0.85 V	0.5 V	0.484 ± 0.002 V
Negative Equilibrium Potential	−0.53 V	−0.46 V	−0.553 ± 0.006 V

The simulation results in this paper closely match the experimental results from the study in [21]. However, the UV irradiation position in that paper differs from the one used in this study. In future work, we will use the same irradiation method to compare our

simulation results with real experimental values. We will optimize the EH and test quality using optical parameters and physical characteristics.

4. Conclusions

This paper introduces a comprehensive charge management simulation model tailored to accommodate various irradiation techniques within a UV charge management system. Initially, a detailed three-dimensional model of the TM and EH was constructed, incorporating realistic surface physical properties derived from LPF experimental data. Subsequently, ray tracing simulations were conducted to compute the photon flux distribution on the surfaces of the TM and EH. By analyzing the kinetic energy, polar angle, and azimuthal angle distributions of the photoelectrons, their trajectories within the EH were meticulously tracked to quantify the charging and discharging rates of the TM.

Utilizing the aforementioned model, the influence of TM displacement on the discharge performance of the charge management system was thoroughly analyzed. Simulation results indicate that the charge management system's performance with the TM in an extreme offset position can deviate by more than 15% compared to its performance when the TM is near the central position. However, a displacement within 0.1 mm exhibits no significant impact on system performance. Furthermore, simulations of the TM's charging and discharging processes under varying initial charge conditions revealed the influence of surface potential on the TM during these processes. The simulation results demonstrate that under the specified illumination conditions, the TM's maximum discharging rate can reach 2.3 mV/s, while the maximum charging rate can attain 0.88 mV/s. The positive equilibrium potential stabilized at approximately 0.85 V, whereas the negative equilibrium potential stabilized around -0.53 V. Currently, our simulation model has been limited to testing the DC discharge performance of the charge management system, without yet incorporating more complex alternating current discharge models. At the same time, the model we have currently established still simplifies certain complex conditions and does not account for factors such as the Patch effect and variations in quantum yield in the actual charge management system that could impact system performance.

The simulation framework developed in this study successfully replicated the TM's charging and discharging rates under the illumination of a DC-driven UV lamp within a ground-based torsion pendulum charge management system, offering a valuable reference for future system design. In future work, we plan to conduct further experiments, including the investigation of non-uniform work function distributions and quantum yield effects on the charge management system's performance, as well as modeling the charging and discharging processes under alternating current discharge conditions to more comprehensively characterize the operational state of the inertial sensors.

Future enhancements should consider changes in the surface physical properties of the TM and EH under more varied conditions to more accurately simulate the charge management system's performance. Additionally, the TM's charging and discharging rates should be evaluated under more complex scenarios to validate the charge management simulation model. Finally, we aim to optimize the UV light source positioning within the simulation model, assess the TM's charging and discharging performance under various UV light sources, and implement additional strategies to further improve the charge management system's efficiency. As this research advances, it will contribute to the design of a more robust charge management system, suitable for future high-precision measurement applications.

Author Contributions: Conceptualization, Z.Z.; methodology, T.Y.; software, Z.Z., S.W. and H.L.; validation, Z.Z.; formal analysis, Z.Z.; investigation, Z.Z. and T.Y.; resources, T.Y. and Z.W.; data curation, Z.Z.; writing—original draft preparation, Z.Z.; writing—review and editing, Z.Z. and T.Y.; visualization, Z.Z.; supervision, T.Y. and Z.W.; project administration, T.Y. and Z.W.; funding acquisition, T.Y. and Z.W. All authors have read and agreed to the published version of the manuscript.

Funding: This research was funded by the National Key R&D Program of China, grant number 2020YFC2200604, and the National Key R&D Program of China, grant number 2020YFC2200600.

Data Availability Statement: Dataset available on request from the authors.

Conflicts of Interest: The authors declare no conflicts of interest.

Abbreviations

The following abbreviations are used in this manuscript:

TM	Test mass
EH	Electrode housing
UV	Ultraviolet
LPF	LISA Pathfinder
LED	Light-Emitting Diode
DC	Direct current
PDF	Probability density function

Appendix A

Table A1 provides the meanings of the symbols used in the equations within this paper for the convenience of the readers.

Table A1. Comparison table of the meanings of symbols in the formulas within the text.

Equation	Symbols	Meaning of Symbols
Equation (1)	$P(r)$	Power distribution
	P_0	The maximum optical power
	r	The radial distance from the center
	γ	The Gaussian radius
Equation (2)	E	The initial kinetic energy of the photoelectron upon escape
	E_m	The maximum initial kinetic energy the photoelectron can have
	$c_1 = c\frac{4\pi m}{h^3}$	c is a parameter related to factors such as incident light frequency and intensity, with a value of $0 < c < 1$, where h is Planck's constant and m is the electron mass
	ω	A parameter related to the metal reflection effect
	T	The absolute temperature
	k	The Boltzmann constant
	e	The natural constant
Equation (3)	θ	The polar angle of the photoelectron at the time of emission
	$\mu = \frac{E_m}{kT}$	Symbols in the current formula have the same meaning as in the previous formula
		The remaining symbols have the same meaning as the corresponding symbols in Equation (2)
Equation (4)	$PDF_{dx,dy}$	The PDF of the photon flux distribution on the conductor surface
	$f(dx, dy)$	The discrete distribution function of the photon flux on the conductor surface
	PF_{total}	The total photon flux on the conductor surface
Equation (5)	V_0	The velocity of the photoelectron upon emission
	E	The initial kinetic energy of the photoelectron upon escape
	m	The mass of the photoelectron
Equation (6)	V_{0x}, V_{0y}, V_{0z}	The velocities of the photoelectron in the x, y, and z directions
	θ	Polar angle
	φ	Azimuth angle
Equation (7)	N_e	The number of photoelectrons
	N_p	The number of photons incident on the conductor surface
	QY_{ext}	The quantum yield
Equation (8)	E_z	The kinetic energy of the photoelectron in the z direction
	m	The mass of the photoelectron
	V_{0z}	The velocities of the photoelectron in the z directions

Table A1. *Cont.*

Equation	Symbols	Meaning of Symbols
Equation (9)	$E_{z'}$	The number of photoelectrons
	e	The charge
	U_D	The potential difference between the TM and the EH
Equation (10)	t	The time for the photoelectron to travel between the TM and the EH
	s	The distance between the TM and the EH
	V_{0z}	The velocities of the photoelectron in the z directions
Equation (11)	S_x, S_y	The displacement of the photoelectron in the x and y directions
	V_{0x}, V_{0y}	The velocities of the photoelectron in the x and y directions
	t	The time for the photoelectron to travel between the TM and the EH
Equation (12)	x_0, y_0	The initial generation position of photoelectrons
	S_x, S_y	The displacement of the photoelectron in the x and y directions
	x_{tm}, y_{tm}	The corner position coordinates of the TM
Equation (13)	U_D	The potential difference between the TM and the EH
	U_{TM}	The surface potential of the TM
	U_{EH}	The surface potential of the EH

References

1. Armano, M.; Audley, H.; Baird, J.; Binetruy, P.; Born, M.; Bortoluzzi, D.; Castelli, E.; Cavalleri, A.; Cesarini, A.; Chiavegato, V.; et al. In-depth analysis of LISA Pathfinder performance results: Time evolution, noise projection, physical models, and implications for LISA. *Phys. Rev. D* **2024**, *110*, 042004. [CrossRef]
2. Luo, J.; Bai, Y.Z.; Cai, L.; Cao, B.; Chen, W.M.; Chen, Y.; Cheng, D.C.; Ding, Y.W.; Duan, H.Z.; Gou, X.; et al. The first round result from the TianQin-1 satellite. *Class. Quantum Gravity* **2020**, *37*, 185013. [CrossRef]
3. Yue-Liang, W.; Zi-Ren, L.; Jian-Yu, W.; Meng, B.; Wei, B.; Rong-Gen, C.; Zhi-Ming, C.; Jin, C.; Di-Jun, C.; Ling, C.; et.al. China's first step towards probing the expanding universe and the nature of gravity using a space borne gravitational wave antenna. *Commun. Phys.* **2021**, *4*, 34.
4. Everitt, C.; Muhlfelder, B.; DeBra, D.; Parkinson, B.; Turneaure, J.; Silbergleit, A.; Acworth, E.; Adams, M.; Adler, R.; Bencze, W.; et al. The Gravity Probe B test of general relativity. *Class. Quantum Gravity* **2015**, *32*, 224001. [CrossRef]
5. Touboul, P.; Métris, G.; Rodrigues, M.; André, Y.; Baghi, Q.; Berge, J.; Boulanger, D.; Bremer, S.; Chhun, R.; Christophe, B.; et al. Space test of the equivalence principle: First results of the MICROSCOPE mission. *Class. Quantum Gravity* **2019**, *36*, 225006. [CrossRef]
6. Antonucci, F.; Armano, M.; Audley, H.; Auger, G.; Benedetti, M.; Binetruy, P.; Bogenstahl, J.; Bortoluzzi, D.; Bosetti, P.; Brandt, N.; et al. The LISA pathfinder mission. *Class. Quantum Gravity* **2012**, *29*, 124014. [CrossRef]
7. Everitt, C.; Parmley, R.; Taber, M.; Bencze, W.; Burns, K.; Frank, D.; Kolodziejczak, J.; Mester, J.; Muhlfelder, B.; Murray, D.; et al. Gravity Probe B cryogenic payload. *Class. Quantum Gravity* **2015**, *32*, 224009. [CrossRef]
8. Grimani, C.; Villani, M.; Fabi, M.; Cesarini, A.; Sabbatini, F. Bridging the gap between Monte Carlo simulations and measurements of the LISA Pathfinder test-mass charging for LISA. *Astron. Astrophys.* **2022**, *666*, A38. [CrossRef]
9. Grimani, C.; Villani, M.; Fabi, M.; Sabbatini, F. LISA and LISA-like mission test-mass charging for gamma-ray burst detection. *J. High Energy Astrophys.* **2024**, *42*, 38–51. [CrossRef]
10. Armano, M.; Audley, H.; Baird, J.; Binétruy, P.; Born, M.; Bortoluzzi, D.; Castelli, E.; Cavalleri, A.; Cesarini, A.; Cruise, A.M.; et al. Charging of free-falling test masses in orbit due to cosmic rays: Results from LISA Pathfinder. *Phys. Rev. D* **2023**, *107*, 062007. [CrossRef]
11. Vocca, H.; Grimani, C.; Amico, P.; Gammaitoni, L.; Marchesoni, F.; Bagni, G.; Marconi, L.; Stanga, R.; Vetrano, F.; Vicere, A. Simulation of the charging process of the LISA test masses due to solar particles. *Class. Quantum Gravity* **2005**, *22*, S319. [CrossRef]
12. Han, R.; Cai, M.; Yang, T.; Xu, L.; Xia, Q.; Jia, X.; Gao, D.; Han, J. Effect of solar proton events on test mass for gravitational wave detection in the 24th solar cycle. *Sci. Rep.* **2023**, *13*, 9932. [CrossRef] [PubMed]
13. Rui-Long, H.; Ming-Hui, C.; Tao, Y.; Liang-Liang, X.; Qing, X.; Jian-Wei, H. Mechanism of cosmic ray high-energy particles charging test mass. *Acta Phys. Sin.* **2021**, *70*, 229501.
14. Chen, H. The Charge Management Research in the Torsion Pendulum. Master's Thesis, Huazhong University of Science & Technology, Wuhan, China, 2013.
15. Rowan, S.; Twyford, S.; Hutchins, R.; Hough, J. Investigations into the effects of electrostatic charge on the Q factor of a prototype fused silica suspension for use in gravitational wave detectors. *Class. Quantum Gravity* **1997**, *14*, 1537. [CrossRef]
16. Mitrofanov, V.; Prokhorov, L.; Tokmakov, K.; Willems, P. Investigation of effects associated with variation of electric charge on a fused silica test mass. *Class. Quantum Gravity* **2004**, *21*, S1083. [CrossRef]
17. Buchman, S.; Quinn, T.; Keiser, G.; Gill, D.; Sumner, T. Charge measurement and control for the Gravity Probe B gyroscopes. *Rev. Sci. Instrum.* **1995**, *66*, 120–129. [CrossRef]

18. Clark, M.; Letson, B.; Parry-Kenyon, S.; Olatunde, T.; Barke, S.; Mueller, G.; Sumner, T.; Wass, P.; Storm, M.; Conklin, J.; et al. A UV LED-Based Charge Management System for the LISA Gravitational Reference Sensor. In Proceedings of the APS April Meeting Abstracts, Virtual, 17–20 April 2021; Volume 2021, pp. K16–002.
19. Yu, T.; Wang, Y.; Liu, Y.; Wang, Z. High-Precision Inertial Sensor Charge Management Based on Ultraviolet Discharge: A Comprehensive Review. *Sensors* **2023**, *23*, 7794. [CrossRef] [PubMed]
20. Hollington, D. The Charge Management System for LISA and LISA Pathfinder. Ph.D. Thesis, Department of Physics, Imperial College London, London, UK, 2011.
21. Fangchao, Y. Investigation of Charge Management and Control for Space Inertial Sensors. Ph.D. Thesis, Huazhong University of Science & Technology, Wuhan, China, 2020.
22. Ziegler, T.; Bergner, P.; Hechenblaikner, G.; Brandt, N.; Fichter, W. Modeling and performance of contact-free discharge systems for space inertial sensors. *IEEE Trans. Aerosp. Electron. Syst.* **2014**, *50*, 1493–1510. [CrossRef]
23. Sala, L. Residual test Mass Acceleration in LISA Pathfinder: In-depth Statistical Analysis and Physical Sources. Ph.D. Thesis, Università degli studi di Trento, Trento, Italy, 2023.
24. Sumner, T.J.; Mueller, G.; Conklin, J.W.; Wass, P.J.; Hollington, D. Charge induced acceleration noise in the LISA gravitational reference sensor. *Class. Quantum Gravity* **2020**, *37*, 045010. [CrossRef]
25. Yang, Q. Research on the Fiber Coupling of Ultraviolet Light Source in Charge Management. Master's Thesis, Huazhong University of Science & Technology, Wuhan, China, 2020.
26. Liu, R.; Zhao, S.; Gu, Y.; Xie, R.; Zhao, M. Design of fiber array collimator and measurement of its divergence angle. *Opt. Precis. Eng.* **2023**, *31*, 89–98.
27. Hechenblaikner, G.; Ziegler, T.; Biswas, I.; Seibel, C.; Schulze, M.; Brandt, N.; Schöll, A.; Bergner, P.; Reinert, F.T. Energy distribution and quantum yield for photoemission from air-contaminated gold surfaces under ultraviolet illumination close to the threshold. *J. Appl. Phys.* **2012**, *111*, 124914. [CrossRef]
28. Chuan-Teh, W. Initial energy distribution and angular distribution of photoelectrons. *Acta Phys. Sin.* **1958**, *14*, 139. [CrossRef]